

AAT Imaging and Microslit Spectroscopy in the Southern Hubble Deep Field

Karl Glazebrook^{1,2}, Aprajita Verma^{3,4}, Brian Boyle^{5,2}, Sebastian Oliver^{3,6}, Robert G. Mann^{3,7}, Davienne Monbleau²

ABSTRACT

We present a deep photometric (B - and R -band) catalog and an associated spectroscopic redshift survey conducted in the vicinity of the Hubble Deep Field South. The spectroscopy yields 53 extragalactic redshifts in the range $0 < z < 1.4$ substantially increasing the body of spectroscopic work in this field to over 200 objects. The targets are selected from deep AAT prime focus images complete to $R < 24$ and spectroscopy is 50% complete at $R = 23$. There is now strong evidence for a rich cluster at $z \simeq 0.58$ flanking the WFPC2 field which is consistent with a known absorber of the bright QSO in this field. We find that photometric redshifts of $z < 1$ galaxies in this field based on HST data are accurate to $\sigma_z/(1+z) = 0.03$ (albeit with small number statistics). The observations were carried out as a community service for Hubble Deep Field science, to demonstrate the first use of the ‘nod & shuffle’ technique with a classical multi-object spectrograph and to test the use of ‘microslits’ for ultra-high multiplex observations along with a new VPH grism and deep-depletion CCD. The reduction of this new type of data is also described.

Subject headings: Catalogs, surveys, Galaxies: evolution

1. Introduction

The Hubble Deep Field South (HDF-S) is one of the deepest imaging fields in the sky. It was observed in 1998 (Williams et al. 2000) by the Hubble Space Telescope (HST) as a counterpart to the northern Hubble Deep Field (HDF-N). However in contrast to the northern field it was selected to

contain a bright QSO J2233-606 at $z = 2.24$ in order to facilitate studies of the connection between foreground galaxies and absorbing systems in the QSO spectrum.

The determination of precise redshifts for extragalactic sources has been important since the time of Hubble (1929). While much spectroscopy has been done in the other Hubble Deep Field, HDF-S has lagged behind. As a community service and in order to test new instrumentation techniques, in particular ‘nod & shuffle’ (Glazebrook & Bland-Hawthorn 2001; GB01) with very small ‘microslits’, we carried out a spectroscopic campaign of galaxies in, and in the vicinity of, the HDF-S in order to obtain redshifts. The plan of this paper is as follows: Section 2 details the prime focus pre-imaging, the procedures used to construct the photometric catalog and the selection of the spectroscopic targets. In Section 3 we describe our novel spectroscopic observations and the special data reduction procedures used. In Section 4 we present our spectroscopic catalog and its basic pa-

¹Department of Physics and Astronomy, Johns Hopkins University, Baltimore, MD 21218

²Anglo-Australian Observatory, P.O.Box 296, Epping NSW, Australia

³Astrophysics Group, Imperial College London, Blackett Laboratory, Prince Consort Road, London, SW7 2AZ, UK

⁴Max-Planck-Institut für extraterrestrische Physik, Giessenbachstraße, 85748 Garching, Germany

⁵Australia Telescope National Facility, PO Box 76, Epping NSW 1710, Australia

⁶Astronomy Centre, University of Sussex, Falmer, Brighton BN1 9QJ, UK

⁷Institute for Astronomy, University of Edinburgh, Royal Observatory, Blackford Hill, Edinburgh EH9 3HJ, UK

rameters and compare with other work in this field and discuss the possible galaxy cluster at $z \simeq 0.58$.

The finding charts, images, spectra, photometric and spectroscopic catalogs presented in this paper are all available from the Anglo-Australian Observatory web site at:

<http://www.aao.gov.au/hdfs/Redshifts>

2. Imaging Observations & Spectroscopic Selection

We obtained pre-imaging data¹ (prior to the HST campaign) from which our sample of targets for spectroscopic follow-up were selected. Images in B and R were taken with the Anglo Australian Telescope Prime Focus CCD camera (0.391"/pixel) in May 1999 at two pointings containing the WFPC ('AAT-WF') and STIS ('AAT-ST') fields respectively. When stacked and mosaicked, they cover a contiguous area of $12.5' \times 7'$ centered on $22^{\text{h}} 33^{\text{m}}18.68^{\text{s}} -60^{\circ}31'45.8''$ (J2000) which includes the HST deep fields and their flanking fields. All images were taken in photometric conditions and $0.8''$ seeing, except for the B -band AAT-ST data ($2.2''$ through thick clouds). A finding chart for our pointing is given in Figure 1.

The images were de-biased, flat-fielded and mosaiced following standard CCD procedures. All images were registered to the USNO-A2.0 reference frame using x- and y-shifts and rotation. The internal astrometric offset between sources in overlapping frames is measured to be $\approx 0.12''$. An all-sky photometric solution was determined from observations of 7 Landolt (1992) fields using 29 stars. B -band images taken in non-photometric conditions and were calibrated using overlap areas with photometric images (accurate to < 0.04 mags residual scatter). A source catalogue was extracted using SExtractor version 2.2.1 (Bertin and Arnouts, 1996). SExtractor was run in the standard manner using a low detection threshold of 1σ and a minimum of 3 connected pixels to define the extraction. We used a local determination from the sky to accurately handle data with variable sky levels. This is particularly important since the images suffer from strong stray light pollution from an off-image star to the north of the field (HD

213479 at $22^{\text{h}} 33^{\text{m}}10.97^{\text{s}} -60^{\circ}26'00.4''$, $B=8.1$). In order to maximise the reliability of the final catalogue without compromising the faint source detection, we flagged sources which lie in areas most strongly affected by straylight or in vignetted regions as 'masked' to minimise the number of spurious extractions. Only sources lying within unmasked regions are considered as targets and for further analysis. The magnitudes presented in the final catalogue are SExtractor MAG_AUTO magnitudes determined using an automated adaptive aperture technique. The final photometric catalog is given in Table 1 (electronic edition only).

We extracted an extragalactic catalogue using star-galaxy separation and analysed the resulting extragalactic number counts. We chose to use the object's magnitude and a measure of surface brightness (magnitude/FWHM²) as our star-galaxy separator as it provides a cleaner cut at faint magnitudes than SExtractor's classifier or the commonly used core:total indicator. Our number-magnitude analysis showed the counts of galaxies to be still increasing as a power-law to $R=24$, consistent with close to 100% completeness at this depth. The formal magnitude limit of the images, measured from the noise in random $0.8''$ diameter apertures placed on blank regions is $R=25.30$, 25.16 (WF, ST) for a 3σ detection. This is also consistent with the images being highly complete at $R = 24$. The B -data reaches 25.18 (WF) and 23.97 (ST, $2''$ aperture — due to the poorer seeing). At $R = 24$ galaxies overwhelmingly dominate stars and so we chose to select spectroscopic targets from a purely R magnitude limited catalog to this depth. $R = 24$ was somewhat deeper than we expected to reach with spectroscopy even under the best conditions, however we expected to go deeper for objects with strong emission lines and we also desired a high surface density to test the 'microslit' spectroscopy described below so our final strategy was to observe a lot of objects and tolerate a lower completeness. The final list of objects that made it on to the slit-mask was based solely on geometrical considerations.

Finally, we note that the spectroscopic selection was done on a preliminary version of the final astrometric and photometric table presented here. We find that the positions and magnitudes reproduce well between the preliminary catalog and the

¹We briefly describe the imaging here and further details are given on the project website.

final version (< 0.4 arcsec and < 0.03 mag systematic differences).

3. Spectroscopic Observations

The spectroscopic observations were made with the Anglo-Australian Telescopes Low Dispersion Survey Spectrograph (Wynne & Worswick 1988). This instrument (LDSS) was designed for multi-slit imaging spectroscopy and offers a wide circular (12.3 arcmin diameter) field of view. Data was taken in October 1998 during a commissioning run to test the following new features:

1. A new deep-depletion CCD detector from MIT Lincoln Labs (see Burke et al. 2004 for details on these devices) had just been installed offering improved red sensitivity. The deep depletion of high-resistivity p-type Silicon causes pixels to be up to $40\mu\text{m}$ deep, this allows more depth for a photon to be detected and improves the quantum efficiency $> 8000\text{\AA}$ where Silicon is becoming increasingly transparent. It also reduces the effect of fringing. We obtained a 2048×4096 pixel device ($15\mu\text{m}$ pixels giving 0.395 arcsec / pixel). The red quantum efficiency peaked at 87% at 7000\AA and maintained 16% at $10,000\text{\AA}$. (Tinney & Barton 1998).
2. A new red-optimized grism based on a Volume Phase Holographic (VPH) grating from Kaiser Optical Systems was tested. VPH gratings offer improved throughput (Barden et al. 1998). This was the first test of a low-resolution VPH grating designed for redshift measurements in a multi-object system and proved successful. The peak efficiency was measured to be 82% at 6700\AA (Glazebrook 1998). The grating delivered a dispersion of 2.6\AA per pixel with the MIT/LL CCD and a one arcsec slit projected to ~ 3 pixels giving 8\AA spectral resolution.
3. The use of ‘nod & shuffle’ (GB01) for accurate sky-subtraction for the first time in a multi-object configuration.
4. The use of very small slits (‘microslits’), enabled by nod & shuffle, to allow large multiplex, as described below.

3.1. Nod & Shuffle

The nod & shuffle technique for highly accurate sky-subtraction is extensively described in GB01. In a nutshell the technique uses an unilluminated part of the CCD as a storage area for an image of the sky. Observing consists of taking an image of the objects through the slits, clocking the CCD voltage pattern so this image is ‘shuffled’ in to the storage, nodding a few arcsecs, taking an image of the sky through the slits, and repeating. The result is quasi-simultaneous images of the object and sky adjacent on the CCD. This is done rapidly to track sky variations, e.g. for HDF-S we took 30 sec images at object and sky positions (plus a 2 sec deadtime to allow for telescope settling). The sequence is repeated $30\times$ giving an 1800 sec (900 sec on object) exposure. Readout noise only becomes important during the final clock-out, charge shuffling is essentially noiseless as long as the CCD has good charge-transfer efficiency (CTE). Sky-subtraction then consists of windowing the sky region of the image and then subtracting it from the object region which is offset by an exactly known number of pixels. With the setup employed here the systematic sky residuals do not exceed 0.04% (measured in GB01).

Many schemes are possible for laying out positions of slits and storage areas on the detector. Whether one can shuffle a long distance or a short distance depends on the CTE and the number of charge traps on the detector (each trap causes a trail of charge when shuffled). For example Abraham et al. (2004) in their later Gemini Multi-Object Spectrograph (GMOS) observations used 2 arcsec long rectangular slitlets, and ‘microshuffled’ the charge only one slit length. The storage was immediately below the detector so effectively 50% of the GMOS FOV was available to slits. For these small shuffles CTE is not critical, also the GMOS CCDs had hundreds of charge traps so small shuffles was desirable.

For our observations the MITLL3 CCD only had 12 traps and the CTE was 99.9999% which allowed us to make large ‘macroshuffles’ across the whole device. We chose to follow the scheme shown in Figure 2 which is motivated by the fact that the MITLL3 device is physically much larger than the LDSS focal plane. One third of the device (1365 pixels = 9.0 arcmin) is used for imag-

ing, the rest for storage. 75% of the LDSS FOV is available for slits, which is advantageous, but we have to shuffle 1365 pixels. This is not a problem with the high CTE, tests in the lab showed significant image degradation did not happen until several hundred macroshuffle operations had been performed. Finally, we note that the FOV advantage in macroshuffling is only gained when the FOV greatly underfills the CCD and would not be applicable, for example, to GMOS.

3.2. Microslits & Mask design

The unconventional approach taken with the spectroscopic masks was that instead of using rectangular slitlets we used small circular holes in the mask at the location of target galaxies. The logic was that the usual reason to employ an extended rectangular slit several arcsecs long is to sample neighboring sky for sky-subtraction. With the nod & shuffle technique this need is obviated. Thus one only needs apertures large enough to receive the light from typical targets in the expected seeing. Normal LDSS slitlets are of order 5–10 arcsec in length, thus with 1 arcsec ‘microslits’ we could obtain a 5–10 \times larger multiplex.

Ideally we would have used square holes so that the spectral PSF would be uniform across the target but due to hardware limitations of our particular mask cutter it turned out to be much easier to simply drill circular holes. The PSF variation is not important for one dimensional spectra summed across the slit and does not affect nod & shuffle sky subtraction as objects and sky are observed through exactly the *same* slits (this is confirmed by the essentially Poisson-limited sky subtraction in the final spectra). Note we planned to do the observations in the best AAT seeing ($\lesssim 1$ arcsec) and so we cut one arcsec holes (150 μm diameter). The masks were available immediately before the run but there was no opportunity to measure them until after the run. Using a microscope we later measured the diameters to be on average 0.7 arcsec, this would have resulted unfortunately in light loss given the actual seeing. This non-optimal size lessened our final spectroscopic depth.

Slit allocation was done using a custom algorithm which simply maximizes the number of non-overlapping target spectra for a given position angle. We chose 90° (i.e. along the STIS-WFPC2

axis) in order to maximize the number of targets allocated within the Hubble camera fields. We found the typical overall number of slits allocated by our algorithm was not sensitive to this choice. The position angle is not optimal for atmospheric dispersion, however since we were doing red spectroscopy this would not have been a significant source of light loss. Using the red VPH grating the 2048 pixels in the dispersion (CCD row) direction gives 5300Å wavelength coverage. The typical wavelength range observed for a slit on the mask center was 5000–10000Å. Slits were allowed to be as far as 1.5 arcmin off-axis resulting in wavelength coverage shifts of up to 590Å. Thus it was only possible to accommodate one object at each CCD row (i.e. one tier). Slit allocation allowed a minimum one pixel gap between objects to cleanly delineate spectra, thus the maximum possible number of holes was 348. Running the algorithm on the $R < 24$ HDF-S catalog for a mask center of $22^h 33^m 11^s -60^\circ 33' 16''$ gave an allocation of 225 objects (after taking out some space to allow for larger holes for alignment stars) in the 3 arcmin \times 9 arcmin field. This compares with a normal LDSS mask setup without nod & shuffle where one normally only gets spectra of 20–30 objects.

The drawback of this strategy is that the objects are out of the slits for half the time when the telescope is in the sky position. An alternate nod & shuffle approach would be to use slightly larger slitlets so the object is still in the slit in both nod positions (e.g. Abraham et al. 2004). However this means in general one can only observe half as many objects because the slits are twice the spatial size, for a *high sky density survey* there is no net difference in the number of objects observed to a given depth in a given amount of telescope time.

3.3. Observations

The observations were carried out over the nights of 13–16th October, 1998 at the AAT. Conditions were photometric and the seeing was 1–1.5 arcsec. The red VPH grating was used with a GG475 blocking filter, so the spectra are potentially contaminated by second order for $> 9000\text{\AA}$, though this effect was not in practice seen in any spectra. The filter was also not anti-reflection coated causing some ghosts in the spectral images.

The total exposure time obtained on the HDF-S field was 12 hours (half on sky). The main calibrations taken were arc spectra for wavelength calibration and white-light dispersed flat fields (through the mask). The flatfields served the dual purpose of removing pixel sensitivity variations and allow the spectra location on the detector to be mapped empirically.

3.4. Data Reduction

The format of the data shares similarities both with classical multislit spectra and with fiber spectra. Each small circular aperture produces a spectral trace (‘tramline’) on the CCD image. A portion of this data is shown in Figure 3. We reduced the data using a mixture of *IRAF* (Tody 1986) tasks and custom *Perl Data Language* (Glazebrook & Economou 1997) scripts. First the individual images were sky-subtracted, using the shuffle offset to map the sky pixels to the object pixels. The images (+ arcs and flats) were then corrected for small alignment shifts throughout the night and registered and stacked with a cosmic ray filter. The flat-field was used to map the spectra tramline locations and also the PSF width as a function of wavelength for optimal extraction of 1D object, sky (for reference), arc and flat-field spectra. The flat-field spectra were then normalized with a polynomial fit in the spectral direction and divided in to the object spectra to correct them for high frequency pixel/wavelength sensitivity variations. An overall wavelength solution was derived from the arc and sky spectra (1Å RMS).

Care was taken to propagate variance arrays (with initial errors calculated from the CCD read-noise and gain using photon statistics) through every step of the data reduction so errors could be assigned to the final spectra.

One important point about the data reduction is that the shuffled sky must be subtracted *before* flat-fielding. This is a key advantage of nod & shuffle: accurate sky-subtraction does not require flat fielding. In the shuffled image the relevant pixel response is that of the original pixel and not the storage pixel. So the correct procedure is to subtract the sky first. The pixel response is the same and the sky subtracts correctly. Then applying the flat field will correct the flat field error in the object correctly. If the flat field is imperfectly measured this only affects the object spec-

trum. Reversing the procedure, i.e. flat fielding before sky subtraction will actually result in an erroneous flat field correction.

4. Spectra and Redshift catalog

Redshifts were determined from the final set of 225 target spectra by careful visual inspection and are given in Table 2 along with key spectral features used for identification and a subjective quality system — $Q = 4$ denotes a dead certain redshift ($> 99\%$ confidence), $Q = 3$ is ‘quite certain’ ($\sim 80\%$ confidence), $Q = 2$ is a ‘possible identification’ ($\sim 50\%$ confidence), $Q = 1$ is a single emission line redshift assumed to be [OII] (which is the best a priori guess given the likely redshift range at $R < 24$ and wavelength coverage) and $Q = 0$ represents no identification.

Out of the 225 objects there were (24, 19, 22, 8, 152) objects with $Q = (4, 3, 2, 1, 0)$ respectively. Thus 73 identifications (33%) were made of which 20 were galactic stars. The completeness was 79%, 63%, 46% at $R < 21, 22, 23$ respectively. Many of the faint $R > 23$ identifications were for objects with strong emission lines. Random example spectra of $Q = 4$ and $Q = 3$ objects are shown in Figure 4 to illustrate the quality. FITS format spectra (and variance spectra) are available on the web site. In the final list we identify five galaxies and two stars within the deep WFPC-2 field and one galaxy in the STIS field.

4.1. Comparison with other HDF-S redshifts

Spectroscopy in the HDF-S vicinity has also been done by Tresse et al. (1999; T99), Vanzella et al (2002; V02) and Sawicki & Mallén-Ornelas (2004; SM03). T99 published redshifts obtained with the NTT for nine objects within 1 arcmin of the QSO with $I < 22.2$, three of these are on our mask of which we identify one (#20) as a star, however this is only a $Q = 2$ confidence. The other two we do not identify. V02 obtained 50 redshifts using the VLT in the range $I_{AB} = 20-25$ (75% complete at $I_{AB} < 22.5$) with an emphasis on color selected $z > 2$ galaxies. We find three identifications in common, all agree at the $\Delta z \leq 0.001$ level. SM03 obtained 97 ‘secure’ redshifts for sources with $I_{AB} < 24$ using the VLT. Five of their objects are also identified by us, all

are high confidence redshifts (except for one single emission line redshift) and all agree to within $\Delta z \leq 0.001$. There is one object (#204) which appears both in V02, SM03 and in our catalog, all at the same redshift. If we exclude the objects in common with the other spectroscopic catalogs we find we have identified 45 new extragalactic objects in the HDF-S and flanking fields. Excluding all objects in common there are now 206 unique galaxies with spectroscopic redshifts from all the HDF-S catalogs considered here.

Another interesting comparison is with catalogs based on photometric redshifts. Here the WFPC-2 field allows accurate photometric redshifts because of the depth and 3 colors. In order to compare we define the fractional error on the redshift as $x = z/(1+z)$, comparing with the catalog of Gwyn (1999) we find that $\sigma_x = 0.03$ between the catalogs (5 galaxies, 2 stars). We also compare with the ‘Stony-Brook’ catalog² which is based on the HDF-N methods of Fernández-Soto et al. (1999). Here we find a big discrepancy in object #871 which Stony-Brook identifies as a star and we identify as a $z = 0.7$ galaxy, albeit with very low confidence ($Q = 2$). Excluding this object we again find $\sigma_x = 0.03$ between the catalogs (4 galaxies, 2 stars).

4.2. Redshift distribution and rich cluster near WFPC2 pointing

The resulting redshift distributions are compared in Figure 5. V02 reported an over-density near the WFPC2 pointing at $z \simeq 0.58$ after combining our data (based on our initial WWW report) with theirs. It can be seen that the redshift spike is at it’s most prominent in our dataset. If we look at the combined redshift distribution in Figure 5 it can be seen that there are a number of spikes, as is typical for narrow field redshift surveys, and that the $z = 0.58$ spike is not the most prominent of them. However the STIS QSO displays a strong absorption line system at $z = 0.570$ (T99) coincident in redshift with a bright spiral galaxy so it is interesting to explore this further. This can be done by looking at the distribution on the sky. Figure 6 shows a comparison of the locations of the galaxies at $0.56 < z < 0.60$ compared

to all the galaxies from this work, SM03, T99 and V02 (after removing all duplicate objects). It is clear that there is a compact cluster of galaxies at this redshift flanking and overlapping with the SW corner of the WFPC2 field. The cluster is of order one arcmin in size which is fairly typical for large clusters at these redshifts. Taking an approximate cluster center of $(-0.5, -0.5)$ arcmin wrt the WFPC2 field we count 16 galaxies within a one arcmin radius and with $0.56 < z < 0.60$. The redshift distribution of galaxies in this circle is shown in the lower half of Figure 6 and it can now be seen that there is again a single prominent spike at $z \simeq 0.58$. Since the overdensity is compact in two dimensions on the sky and also in redshift this is likely to be a cluster rather than a filament of large scale structure. For the 16 galaxies we find $z = 0.574 \pm 0.008$ corresponding to a velocity dispersion $\sigma_v = c\sigma_z/(1+z) = 1500 \text{ km s}^{-1}$. This is typical of a rich cluster of galaxies and we find it is insensitive to the exact choice of radius. These parameters are consistent with the cluster containing the QSO absorber reported by T99 on it’s outskirts.

5. Summary

To summarize the paper:

1. We present a significant new set of photometric and spectroscopic data on the HDF-S.
2. We have demonstrated a new mode of spectroscopic data taking with high-multiplex per unit area on the sky using the technique of ‘microslits’ in conjunction with nod & shuffle.
3. The spectroscopic catalog presented here is the third large catalog of redshifts in the HDF-S and flanking fields. 53 redshifts are obtained of which 45 are new.
4. Comparison with existing photometric redshifts based on WFPC-2 data show these to be in reasonable agreement ($\sigma_z/(1+z) = 0.03$) for $z < 1$ galaxies, albeit with small number statistics.
5. We present strong evidence for a rich cluster, compact in all three spatial dimensions, at

²This data is publicly available from
<http://www.astro.sunysb.edu/astro/hdfs/wfpc2>

$z \simeq 0.58$ flanking the WFPC2 pointing and which very likely contains the known absorbing galaxy of the QSO at this redshift.

Preliminary versions of this catalog have already been used for scientific studies using the HDF-S data. Mann et al. (2002) used it for a study of the relationship between far-infrared and other estimates of galaxy star-formation rates. Vanzella et al. (2002) used this catalog together with theirs to estimate cosmological star-formations rate history. The reader is encouraged to use this catalog for further studies of the HDF-S and its associated QSO.

Based on data from the Anglo-Australian Observatory without whose dedicated staff the LDSS upgrade project could not have proceeded. Nod & shuffle with LDSS was inspired by the pioneering ideas of Joss Bland-Hawthorn to whom KG is indebted for many useful discussions. We would like to especially thank Lew Waller, Tony Farrell and John Barton for their technical work. We would also like to thank Roberto Abraham for his help riding in the AAT Prime Focus cage during these observations, Chris Tinney for observing support, Pippa Goldschmidt for her help with the imaging reductions and Sam Barden (NOAO), Jims Arns and Bill Coulburn (Kaiser) for their help with the VPH grating design and manufacture.

REFERENCES

- Abraham, R. G., et al. 2004, *AJ*, 127, 2455
- Barden, S. C., Arns, J. A., & Colburn, W. S. 1998, *Proc. SPIE*, 3355, 866
- Bertin, E., & Arnouts, S. 1996, *A&AS*, 117, 393
- Burke, B. E., et al. 2004, *Scientific Detectors for Astronomy, The Beginning of a New Era*, eds. Amico, P., Beletic, J. W., Beletic, (Kluwer), 41
- Fernández-Soto, A., Lanzetta, K. M., & Yahil, A. 1999, *ApJ*, 513, 34
- Glazebrook, K. & Economou, F., 1997, *Dr Dobbs Journal*, 1997, 9719 (Fall issue)
- Glazebrook, K. 1998, *AAO Newsletter*, 87, 11
- Glazebrook, K., & Bland-Hawthorn, J. 2001, *PASP*, 113, 197 (GB01)
- Gwyn, S. D. J. 1999, *ASP Conf. Ser.* 191: Photometric Redshifts and the Detection of High Redshift Galaxies, 191, 61
- Hubble, E. 1929, *Proceedings of the National Academy of Science*, 15, 168
- Landolt, A. U. 1992, *AJ*, 104, 372
- Mann R. G., Oliver S., Carballo R., Franceschini A., Rowan-Robinson M., Heavens A. F., Kontizas M., Elbaz D., Dapergolas A., Kontizas E., Granato G. L., Silva L., Rigopoulou D., Gonzalez-Serrano J. I., Verma A., Serjeant S., Efstathiou A., van der Werf P. P., 2002, *MNRAS*, 332, 549
- Sawicki, M., & Mallén-Ornelas, G. 2003, *AJ*, 126, 1208 (SM03)
- Tinney, C. G., Barton, J., 1998, *AAO Newsletter*, 87, 9
- Tody, D. 1986, "The IRAF Data Reduction and Analysis System" in *Proc. SPIE Instrumentation in Astronomy VI*, ed. D.L. Crawford, 627, 733
- Tresse, L., Dennefeld, M., Petitjean, P., Cristiani, S., & White, S. 1999, *A&A*, 346, L21 (T99)
- Vanzella, E., et al. 2002, *A&A*, 396, 847 (V02)
- Williams, R. E., et al. 2000, *AJ*, 120, 2735
- Wynne, C. G., & Worswick, S. P. 1988, *The Observatory*, 108, 161

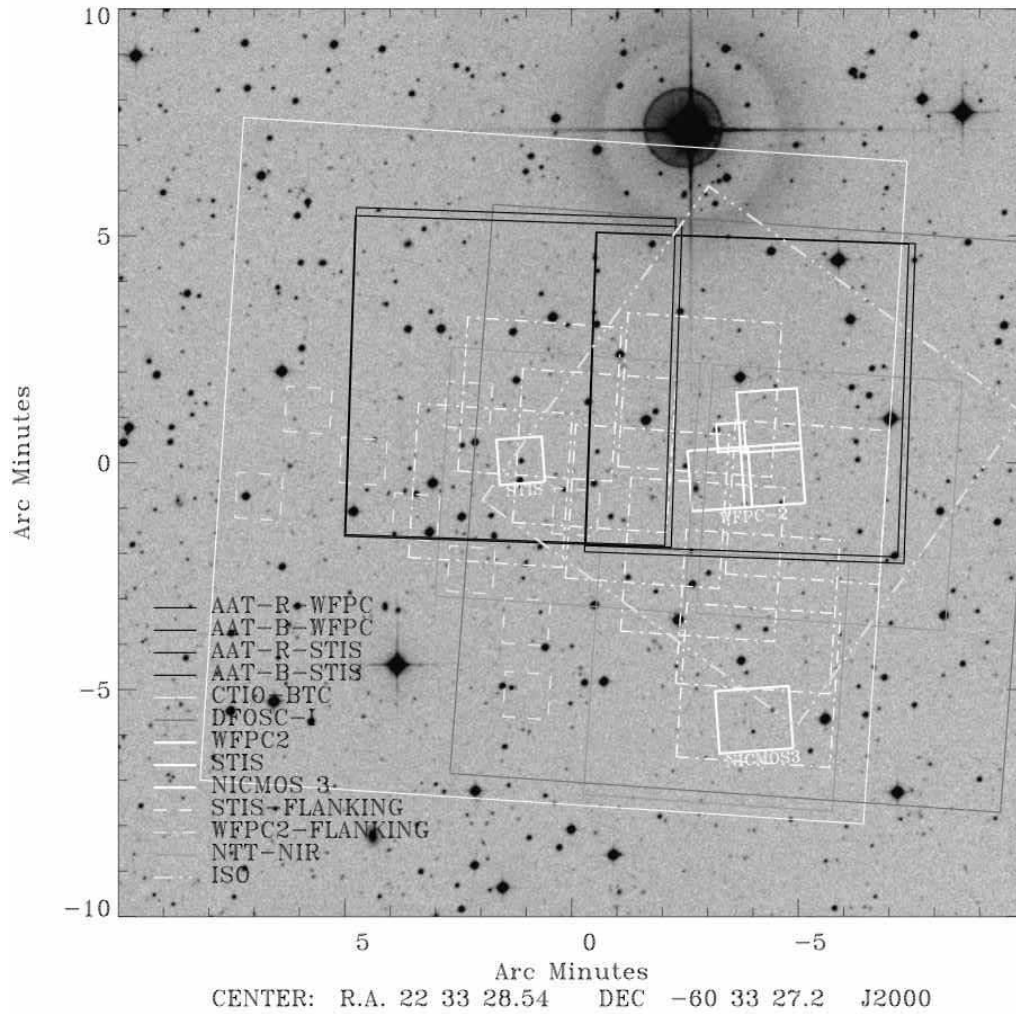


Fig. 1.— Figure depicting follow-up imaging surveys of the HDFs. The extent of the AAT images is shown in black. The bright star HD 213479 which causes stray light in the AAT fields can also be seen.

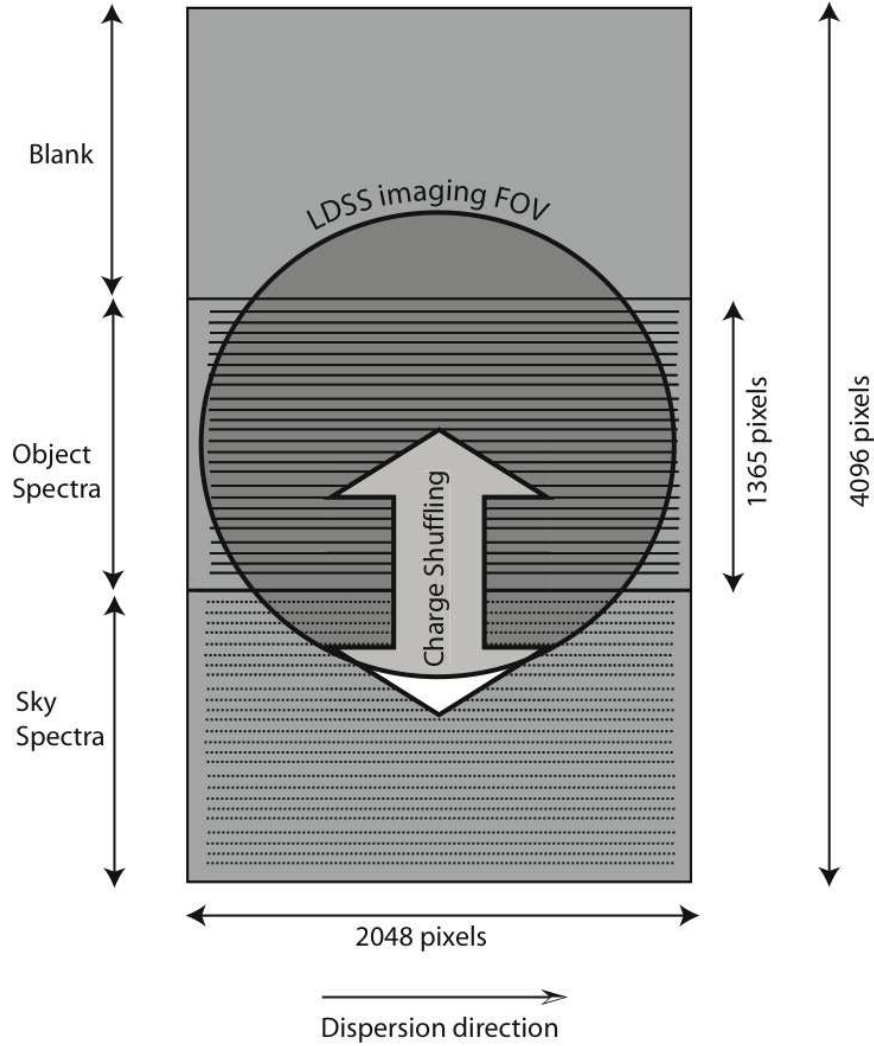


Fig. 2.— Illustration of the particular LDSS nod & shuffle layout we used. The 2048×4096 CCD detector (grey rectangle) is physically larger than the circular image (12.3 arcmin diameter) delivered by the LDSS camera. For nod & shuffle only the middle third of the chip (1365 pixels high) is illuminated by the mask, the lower third is used to store the sky image and the upper third is blank (it hold the object image when the shuffling charge up and down by 1365 pixels). Thus only 9.0 arcmin vertically is available for slits which is almost the full field.

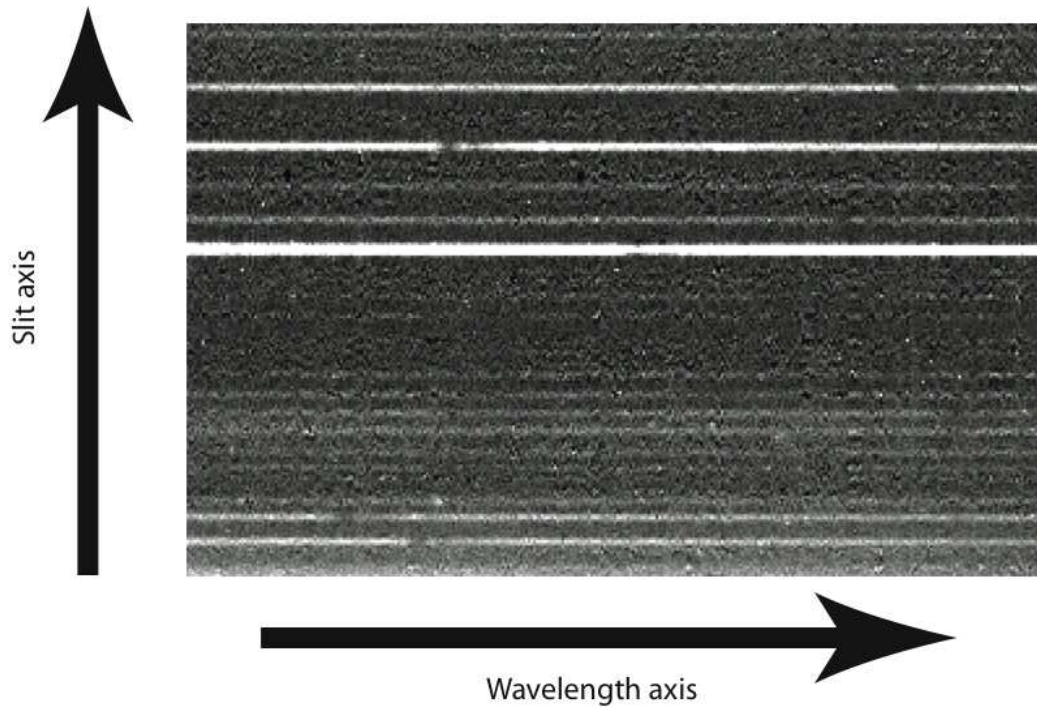


Fig. 3.— Example microslit data. This shows a zoom on a small portion of a 2D data frame (~ 30 microslits) where the only processing applied at this step is the subtraction of the shuffled sky. Each circular microslit produces a spectral trace. Several bright objects with absorption lines and faint objects with emission lines can be seen. The data shares features both with fiber data and classical multislit data. The apertures are unresolved spatially, however unlike fiber data the spacing between apertures is uneven (it reflects the spacing between objects) and the wavelength zeropoints vary too (reflecting the spatial position of the objects on the other axis).

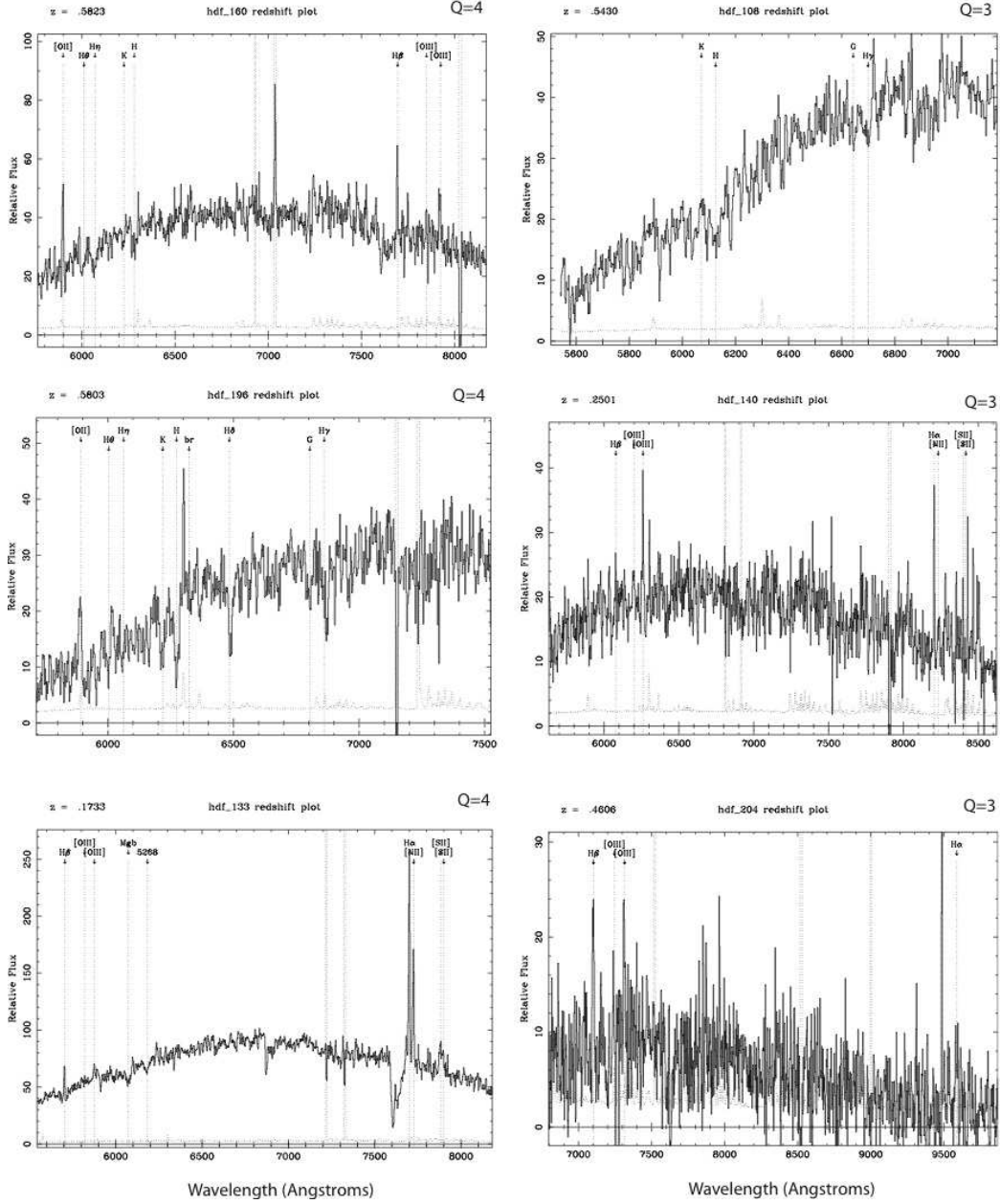


Fig. 4.— Random spectra selected from the survey to illustrate the quality of the spectra. Spectra with $Q = 4$ are shown in the left column and $Q = 3$ are shown in the right column. Identifying spectral features are labeled. The spectra are unfixed and are shown in counts. The dashed line is the 1σ noise amplitude spectrum calculated from the CCD properties.

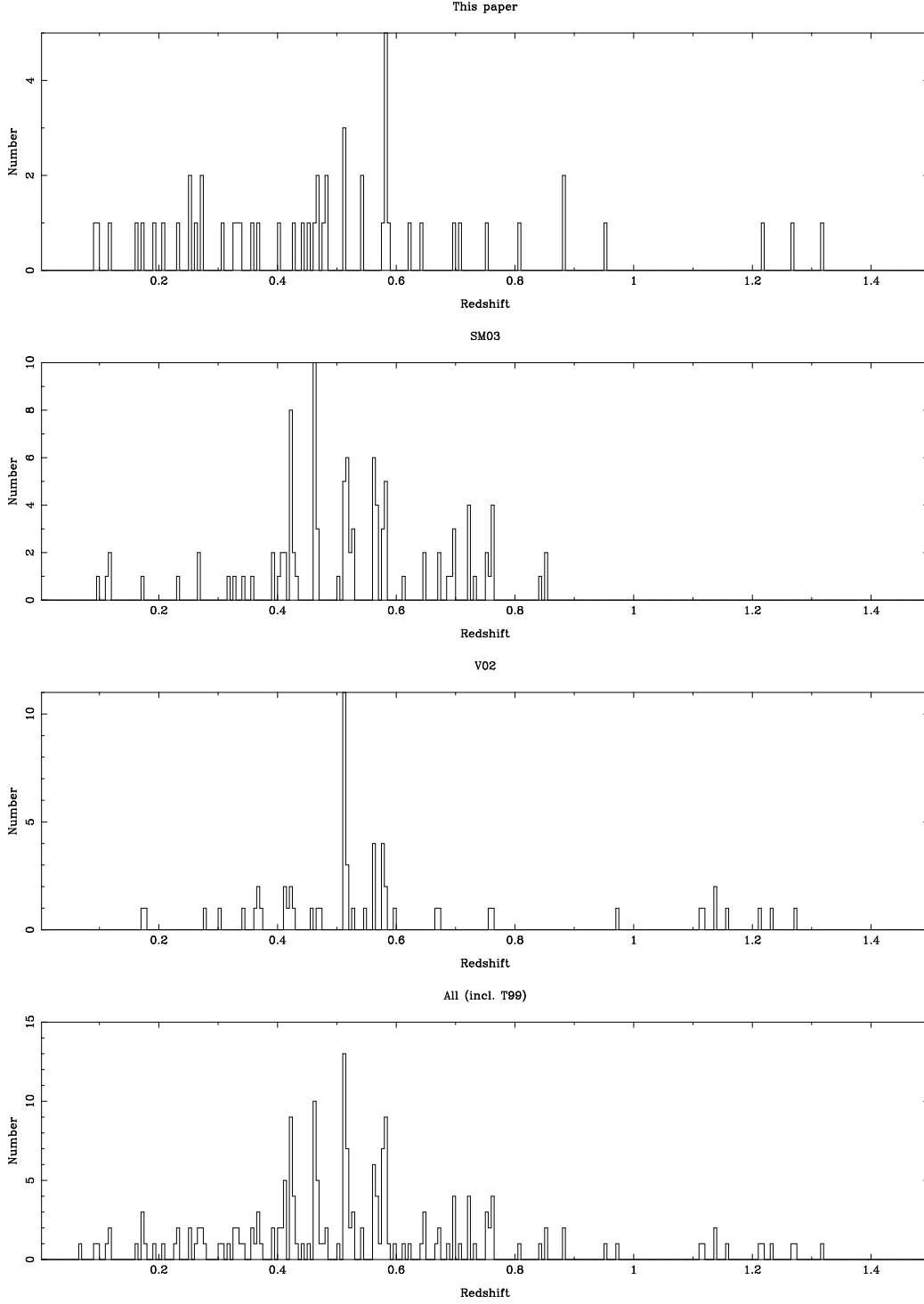


Fig. 5.— Redshift distribution of the HDF-S galaxies in this paper compared with the V02 and SM03 samples. At the bottom the combined redshift distribution (also including the nine T99 objects) is shown (with all objects duplicated between catalogs removed).

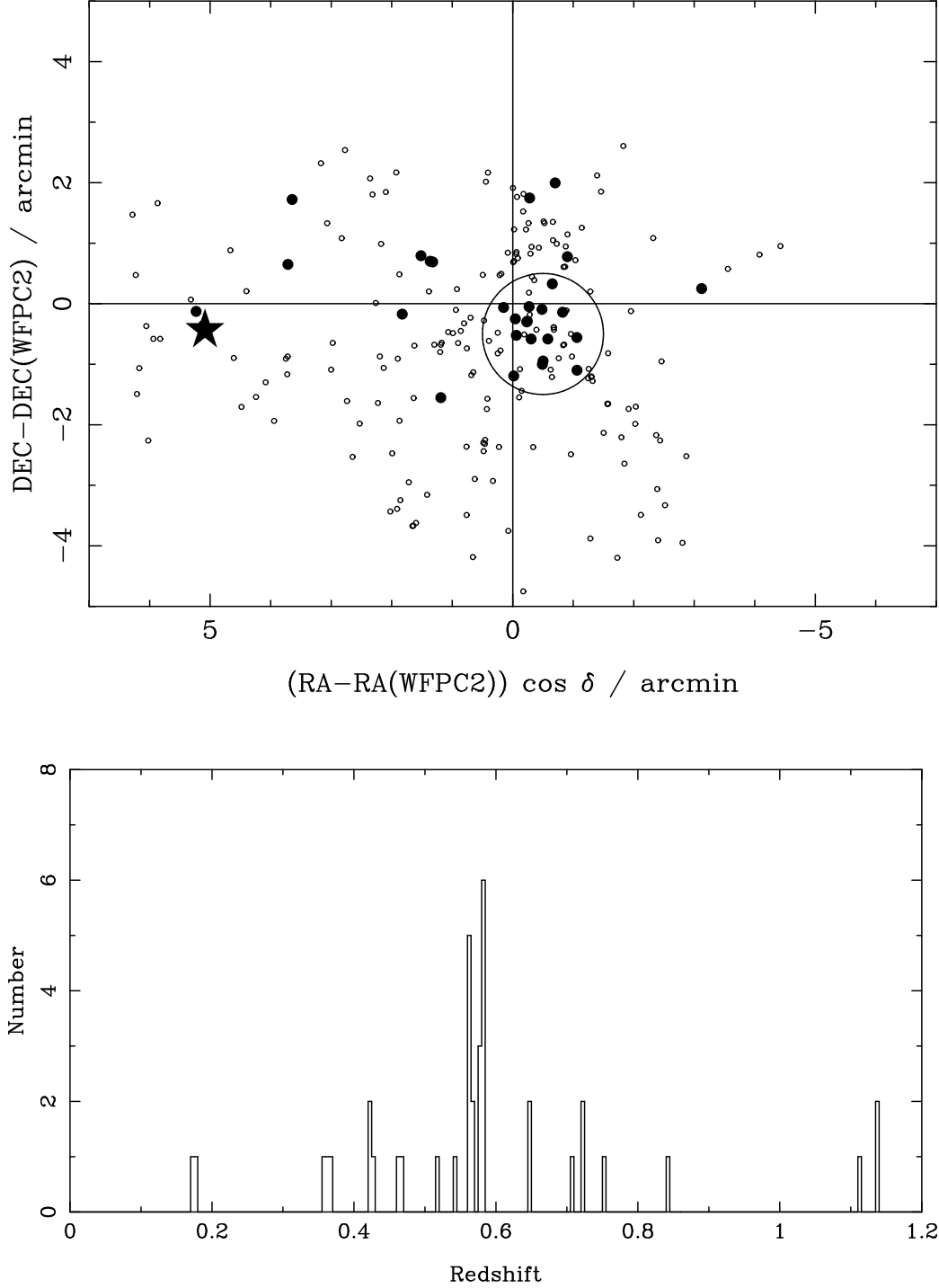


Fig. 6.— Top: Locations of galaxies with $0.56 < z < 0.60$ (solid circles) compared to all galaxies (open circles) with spectroscopic redshifts in the combined sample of this work, T99, SM03, and V02. The circle shows the region used to estimate the velocity dispersion. The position of the STIS QSO is marked with a large star. Bottom: redshift distribution of galaxies within the circle showing the strong spike at $z \simeq 0.58$.

Table 1: Photometric Catalog (electronic edition only)

Phot ID	Coordinates (J2000)	Area ^a	Type Flag ^b	R^c (mag)	R_{err} (mag)	R Class ^d	R Mask ^e	R PHOT ^f	R Flag ^g	B^c (mag)	B_{err} (mag)	B Class ^d	B Mask ^e	B PHOT ^f	B Flag ^g
1	22 32 28.10 -60 34 20.3	WF	G	24.858	0.238	0.670	0	PH	24	-	-	-	-	-	-
2	22 32 28.18 -60 34 9.7	WF	G	25.210	0.264	0.668	0	PH	16	-	-	-	-	-	-
3	22 32 28.25 -60 34 32.9	WF	G	22.840	0.076	0.022	0	PH	24	-	-	-	-	-	-
4	22 32 28.26 -60 33 52.0	WF	G	23.884	0.126	0.025	0	PH	24	-	-	-	-	-	-
5	22 32 28.26 -60 34 39.3	WF	G	22.382	0.059	0.990	0	PH	24	-	-	-	-	-	-
6	22 32 28.31 -60 34 0.9	WF	G	24.186	0.171	0.355	0	PH	24	-	-	-	-	-	-
7	22 32 28.36 -60 35 5.7	WF	G	22.613	0.091	0.147	0	PH	16	-	-	-	-	-	-
8	22 32 28.44 -60 33 9.6	WF	G	22.608	0.048	0.983	0	PH	26	-	-	-	-	-	-
9	22 32 28.48 -60 33 29.8	WF	G	25.237	0.429	0.619	0	PH	16	-	-	-	-	-	-
10	22 32 28.54 -60 34 15.2	WF	G	23.737	0.191	0.685	0	PH	2	-	-	-	-	-	-
11	22 32 28.57 -60 32 43.0	WF	G	24.462	0.222	0.464	0	PH	24	-	-	-	-	-	-
12	22 32 28.66 -60 34 49.7	WF	G	23.862	0.221	0.477	0	PH	0	-	-	-	-	-	-
13	22 32 28.67 -60 33 43.2	WF	G	25.611	0.428	0.666	0	PH	0	-	-	-	-	-	-
14	22 32 28.71 -60 33 57.5	WF	G	24.058	0.214	0.657	0	PH	2	-	-	-	-	-	-
15	22 32 28.72 -60 33 25.2	WF	G	25.763	0.358	0.808	0	PH	0	-	-	-	-	-	-
16	22 32 28.75 -60 32 11.9	WF	G	23.927	0.180	0.782	0	PH	24	-	-	-	-	-	-
17	22 32 28.78 -60 34 4.5	WF	G	25.782	0.228	0.796	0	PH	0	-	-	-	-	-	-
18	22 32 28.80 -60 32 37.9	WF	G	23.950	0.210	0.065	0	PH	16	-	-	-	-	-	-
19	22 32 28.81 -60 33 18.1	WF	G	21.377	0.027	0.382	0	PH	24	-	-	-	-	-	-
20	22 32 28.86 -60 33 59.4	WF	G	24.262	0.222	0.095	0	PH	3	-	-	-	-	-	-
21	22 32 28.94 -60 31 13.6	WF	G	25.251	0.326	0.817	0	PH	24	-	-	-	-	-	-
22	22 32 28.98 -60 34 34.2	WF	G	24.851	0.206	0.930	0	PH	0	-	-	-	-	-	-
23	22 32 29.01 -60 30 55.5	WF	G	25.400	0.240	0.737	0	PH	24	-	-	-	-	-	-
24	22 32 29.02 -60 33 22.4	WF	G	23.591	0.154	0.025	0	PH	0	-	-	-	-	-	-
25	22 32 29.03 -60 33 53.8	WF	G	24.184	0.253	0.508	0	PH	0	-	-	-	-	-	-
26	22 32 29.06 -60 34 14.2	WF	S	23.486	0.082	0.977	0	PH	0	-	-	-	-	-	-
27	22 32 29.08 -60 33 42.0	WF	G	25.011	0.321	0.731	0	PH	0	-	-	-	-	-	-
28	22 32 29.09 -60 30 46.7	WF	G	24.048	0.174	0.339	0	PH	24	-	-	-	-	-	-
29	22 32 29.14 -60 31 6.9	WF	G	23.081	0.095	0.212	0	PH	24	-	-	-	-	-	-
30	22 32 29.14 -60 32 48.6	WF	G	20.725	0.016	0.034	0	PH	0	-	-	-	-	-	-
31	22 32 29.23 -60 32 35.5	WF	G	21.374	0.025	0.983	0	PH	0	-	-	-	-	-	-
32	22 32 29.23 -60 33 33.3	WF	G	23.614	0.116	0.506	0	PH	0	-	-	-	-	-	-
33	22 32 29.23 -60 30 14.2	WF	G	22.472	0.050	0.933	0	PH	24	-	-	-	-	-	-
34	22 32 29.31 -60 34 0.3	WF	G	24.950	0.319	0.534	0	PH	0	23.651	0.099	0.014	0	PH	27
35	22 32 29.32 -60 30 53.8	WF	G	23.176	0.100	0.836	0	PH	16	-	-	-	-	-	-
36	22 32 29.32 -60 31 4.0	WF	G	24.095	0.204	0.631	0	PH	18	-	-	-	-	-	-
37	22 32 29.32 -60 32 11.2	WF	S	21.559	0.036	0.990	0	PH	0	-	-	-	-	-	-
38	22 32 29.33 -60 34 37.1	WF	G	24.646	0.187	0.725	1	PH	0	23.287	0.099	0.011	0	PH	24
39	22 32 29.34 -60 29 53.6	WF	G	24.708	0.184	0.922	0	PH	24	-	-	-	-	-	-
40	22 32 29.35 -60 34 10.3	WF	G	24.263	0.150	0.738	0	PH	0	22.977	0.069	0.010	0	PH	27
41	22 32 29.35 -60 30 10.1	WF	G	24.097	0.168	0.126	0	PH	24	-	-	-	-	-	-
42	22 32 29.37 -60 29 49.9	WF	G	25.378	0.254	0.767	0	PH	24	-	-	-	-	-	-
43	22 32 29.38 -60 33 48.8	WF	G	24.742	0.197	0.847	0	PH	0	22.404	0.055	0.000	0	PH	27
44	22 32 29.43 -60 29 30.7	WF	G	23.845	0.132	0.973	0	PH	24	-	-	-	-	-	-
45	22 32 29.46 -60 31 16.4	WF	G	22.005	0.034	0.986	0	PH	0	-	-	-	-	-	-
46	22 32 29.50 -60 32 43.3	WF	G	22.474	0.046	0.758	0	PH	0	-	-	-	-	-	-
47	22 32 29.53 -60 35 0.3	WF	S	15.535	0.002	1.000	1	PH	15	16.560	0.002	1.000	0	PH	30
48	22 32 29.57 -60 32 29.9	WF	G	23.547	0.126	0.029	0	PH	0	-	-	-	-	-	-
49	22 32 29.57 -60 30 29.3	WF	G	23.894	0.144	0.086	0	PH	2	-	-	-	-	-	-
50	22 32 29.57 -60 30 39.6	WF	G	24.757	0.203	0.870	0	PH	0	-	-	-	-	-	-

Notes: Merged B and R selected catalog. Sample only. Full table accessible from electronic edition and from the WWW at <http://www.aao.gov.au/hdfs/Redshifts>. Dashed entries throughout this table denote missing data primarily due to the B band data being less deep than the R band but also slightly different depth and coverage at the edge of the fields and differences in extraction due to the presence of strong straylight features. This table is not cleaned for sources lying in masked areas (i.e. in vignetted regions or along sites where stray light is strong) but the mask flag is included in the table.

Notes to the column headings:

^a Flag to denote parent image of the detection - WF: AAT-WFPC2 field, ST: AAT-STIS field, WS: Overlap region, WMS: Overlap region but masked in one of the fields.

^b Star/Galaxy indicator as per the classification described in the text S: star G:non-stellar.

^c SExtractor's MAG_AUTO photometry, '-' not-detected.

^d SExtractor's star galaxy classifier - 0: galaxy, 1: star, '-' not-detected.

^e Masked sources are flagged 0, unmasked sources are flagged 1, '-' not-detected.

^f Flag to indicate data taken under photometric conditions 'PH' (WF-B, WF-R, ST-R data) or non-photometric 'NP' where calibration using common sources detected in the photometric (WF-B) and non-photometric (ST-B) lying in the overlap region has been used.

^g SExtractor's output flag, generally <8 is reliable.

TABLE 2
SPECTROSCOPIC REDSHIFT CATALOG.

Slit ID ^a	RA (J2000)	Dec (J2000)	Phot ID ^b	<i>R</i> mag ^c	<i>z</i>	<i>Q</i>	Features ^d , (HDF-S deep coverage)
225	22:32:38.909	-60:34:54.095	472	22.54	9.9999	0	Neg. spectrum. Edge effected.
224	22:32:39.329	-60:31:23.074	488	16.21	0.0000	4	Star
221	22:32:40.078	-60:33:24.599	533	21.43	0.0000	4	Mstar
220	22:32:40.322	-60:33:10.012	545	21.34	0.6213	2	HK, 4000Å
216	22:32:41.357	-60:30:26.276	592	19.27	0.4250	4	OII, Balmer-, HK, H β +
211	22:32:43.392	-60:33:51.782	685	19.91	0.0918	1	Broad line - best guess H α +
207	22:32:44.611	-60:32:45.334	740	23.59	9.9999	0	em line at 5862Å, no cuum
206	22:32:44.873	-60:30:55.537	756	20.01	0.5141	4	HK, 4000Å, G, H γ -, H β -, NaD
204	22:32:45.475	-60:34:19.207	793	21.19	0.4606	3	H β +, OIII(4959+5007)+
197	22:32:47.393	-60:32:00.179	899	21.29	0.0000	4	Mstar (WFPC2)
196	22:32:47.592	-60:33:36.122	912	19.94	0.5803	4	OII, HK, H δ -, G, H γ - (WFPC2)
185	22:32:50.419	-60:34:01.063	1052	17.75	0.0000	4	Mstar (WFPC2)
173	22:32:53.952	-60:31:17.915	1263	20.07	0.5838	2	HK, OII, OIII
170	22:32:54.763	-60:31:13.876	1317	20.74	0.5111	3	HK, 4000
169	22:32:55.022	-60:34:28.999	1331	22.48	0.3562	3	H β +, OIII(4959+5007)
162	22:32:56.890	-60:32:12.142	1432	22.93	0.7525	2	HK, weak abs
160	22:32:57.449	-60:33:06.325	1462	20.57	0.5823	4	OII, Balmer-, HK, G, H β +, OIII (WFPC2)
157	22:32:58.236	-60:33:51.962	1509	22.50	0.7063	2	HK, G, H β + (WFPC2)
156*	22:32:58.706	-60:33:23.818	1532	22.61	9.9999	0	NoID (WFPC2)
155	22:32:59.321	-60:31:19.873	1561	13.60	0.0000	4	Star
154*	22:32:59.554	-60:30:52.744	1578	23.70	0.2706	2	OII, OIII
153	22:32:59.820	-60:31:01.690	1589	23.95	0.1916	3	HK, G, H δ -, H γ -
152	22:33:00.082	-60:33:19.336	1607	23.48	0.5402	2	HK (WFPC2)
145	22:33:02.376	-60:33:46.850	1710	22.56	0.6959	1	OII+ (strong), poss OIII+ (WFPC2)
144	22:33:02.666	-60:32:14.050	1725	18.81	0.0000	4	Mstar
143	22:33:02.974	-60:32:31.589	1741	16.15	0.0000	4	Mstar
140	22:33:03.706	-60:32:48.192	1781	20.66	0.2501	3	H α +, OIII+
133	22:33:05.976	-60:33:50.576	1891	17.20	0.1733	4	H β +, OIII+, Mgb, 5268, H α +, NII+, SII+
128	22:33:07.495	-60:32:50.557	1997	20.17	0.5130	4	HK, H δ -, H β +
127	22:33:08.095	-60:33:22.000	2030	17.13	0.0000	4	Star
126	22:33:08.558	-60:32:15.076	2052	23.59	0.5857	2	OII+, OIII+ (both weak)
123	22:33:09.444	-60:33:44.244	2116	22.12	0.8090	1	strong em line assumd OII. maybe weak abs?
118	22:33:11.078	-60:33:13.043	2229	21.83	0.5815	1	strong em line assumed OII+, maybe wk abs
117	22:33:11.462	-60:32:33.515	2255	21.53	0.4411	2	HK, H δ -, G
116	22:33:11.676	-60:33:57.107	2273	23.17	0.4515	3	HK, H δ -, G
115	22:33:11.866	-60:30:52.632	2292	21.37	0.1633	2	H α -, Mgb, 5268
109†	22:33:13.286	-60:31:11.921	2380	21.56	0.4666	3	HK, 4000Å, also 2nd set of lines z=0.3080 (H β +, OIII+, H α +)!
108	22:33:13.574	-60:34:06.319	2397	18.61	0.5430	3	HK, G, H γ -
107	22:33:14.083	-60:33:55.037	2427	19.95	0.4842	2	HK, G, H γ -
106	22:33:14.292	-60:32:32.687	2774	23.39	9.9999	0	Poss. em line at 7856Å
105	22:33:14.623	-60:33:01.890	2461	22.56	0.4654	2	HK, 4000Å
104	22:33:14.866	-60:31:06.470	2483	23.67	9.9999	0	Contaminated by 103
103	22:33:15.070	-60:31:14.376	2495	20.25	0.3083	3	OII+, H β +, H α +, OIII+
102	22:33:15.394	-60:30:58.532	2521	23.76	0.4760	2	H δ -, G, H γ - (H β - on bad col.) (5861Åabs is contam from 101.)
101	22:33:15.674	-60:32:24.868	2552	13.78	0.0000	4	Mstar
92	22:33:18.499	-60:34:39.112	2730	18.65	0.0991	4	H α +, NII+, SII+
91	22:33:18.782	-60:30:30.373	2743	23.07	0.8839	3	HK, MgII-, FeII-, Misc abs.
90	22:33:19.003	-60:32:27.820	2769	20.66	0.0000	4	Mstar
89	22:33:19.212	-60:31:57.706	2782	22.80	0.3676	2	HK, G, Mgb
85	22:33:20.414	-60:33:41.476	2856	20.61	0.1186	4	H α +, NII+, SII+, H β +, OIII+

TABLE 2—*Continued*

Slit ID ^a	RA (J2000)	Dec (J2000)	Phot ID ^b	<i>R</i> mag ^c	<i>z</i>	<i>Q</i>	Features ^d , (HDF-S deep coverage)
84	22:33:20.633	−60:34:08.094	2863	23.01	1.2184	2	HK, H δ −, 4000Å
83	22:33:20.830	−60:34:35.069	2877	16.93	0.0000	4	Star
82	22:33:21.161	−60:31:42.964	2899	23.23	0.3256	2	HK
79	22:33:22.013	−60:30:43.362	2962	21.00	0.2072	3	HK,G,H β −,Mg
74	22:33:24.018	−60:33:10.605	3088	17.74	0.0000	3	Star
73	22:33:24.216	−60:33:52.908	3102	16.15	0.0000	4	Mstar
67	22:33:25.867	−60:31:19.315	3204	23.05	0.5800	3	OII+,OIII(5007)+
66	22:33:26.221	−60:32:05.943	3229	15.76	0.0000	4	Star
65	22:33:26.480	−60:33:54.955	3249	21.19	0.4802	2	H,K,H β −
64	22:33:26.718	−60:33:57.125	3265	23.56	0.6428	3	H,K,G
59	22:33:28.046	−60:33:38.037	3329	19.79	0.0000	3	Star
58	22:33:28.297	−60:34:58.747	3338	22.98	0.3363	3	OIII(5007+4959)+,H β +,H α +?
57	22:33:28.935	−60:35:01.540	3365	21.36	0.0000	3	Faint Mstar
55	22:33:29.436	−60:34:20.543	3395	23.71	1.3150	1	Single line OII+
54	22:33:30.012	−60:34:01.470	3417	21.27	9.9999	0	Dominated by bizarre negative spectrum - ghost?
52	22:33:30.731	−60:34:35.116	3451	23.47	0.3335	2	Strong OIII 5007+, weak 4959+, H β +, maybe H α +
50	22:33:31.232	−60:33:43.897	3476	19.31	0.0000	4	M-star
48	22:33:31.669	−60:33:41.857	3501	23.87	9.9999	0	Dominated by sky object = bright M star!!
39	22:33:34.176	−60:32:09.698	3616	22.28	0.2304	3	OIII(5007+4959)+, H β +, H α +
31	22:33:37.404	−60:34:03.207	3764	18.67	0.0000	4	M-star
27*	22:33:38.787	−60:33:10.315	3825	23.25	0.5812	2	OII+, wk abs lines (STIS)
25	22:33:39.499	−60:32:58.523	3864	23.15	1.2680	1	Strong line at 8451Å: assumed OII+
20	22:33:41.350	−60:32:56.122	3945	21.24	0.0000	2	H α +,NII+,SII+?
13	22:33:43.962	−60:31:23.017	4069	22.06	0.9534	1	OII+, H β +?
9	22:33:45.029	−60:34:42.559	4117	23.68	9.9999	0	Possible wk em line at 6979Å
8	22:33:45.231	−60:35:18.301	4127	21.98	0.4049	2	OIII+, OII+?, H β +, G
5	22:33:46.169	−60:34:03.448	4169	19.78	0.0000	4	M star
4*	22:33:46.439	−60:34:06.634	4176	23.72	0.2645	2	H α −,Mgb
3*	22:33:46.742	−60:34:32.123	4196	22.60	0.2505	2	H α −,H β −,poss. Mgb and 5268
2*	22:33:46.910	−60:32:34.236	4207	23.33	0.8816	1	Strong line OII+? at 7012Å.
1*	22:33:47.346	−60:31:34.447	4221	21.91	0.2703	3	Broad H β +,H δ +, H θ +, weak (but clear) OIII(5007+4959)+

Note: only objects with IDs ($Q > 0$) are shown. The full table including unidentified objects is available on the web site.

*Spectrum contaminated by scattered light.

†Spectrum appears to contain two superimposed objects at different redshifts.

^aIdentification number in slit mask.

^bIdentification number in photometric catalog (Table 1).

^c*R*-band magnitude (Vega) in preliminary version of photometric catalog used for selection.

^dPrinciple features used to identify spectrum. \pm denotes emission/absorption.